photonics

MDPI

Article

Photosensitive Silicon-Enabled Tunable Terahertz Metasurfaces for Advanced Wavefront Control

Zekun Li [1], Penghui Xin [1], Haoyu Zheng [1], Yu Zheng [1], Leonid F. Chernogor [2], Zhejun Jin [1] and Tian Liu [1,*]

[1] College of Electronic Information, Qingdao University, Qingdao 266071, China; lizekun1@qdu.edu.cn (Z.L.); xinpenghui11@163.com (P.X.); zhenghaoyu@qdu.edu.cn (H.Z.); zhengyu@qdu.edu.cn (Y.Z.); zhejunjin@qdu.edu.cn (Z.J.)

[2] Department of Space Radio Physics, V. N. Karazin Kharkiv National University, 61022 Kharkiv, Ukraine; leonid.f.chernogor@gmail.com

* Correspondence: sdqdlt@qdu.edu.cn

Abstract

Current terahertz (THz) metasurfaces are often constrained by fixed operational states, lacking the flexibility to switch dynamically between transmission and reflection modes. To address this limitation, we propose a tunable coded metasurface based on the photo-adjustable conductivity of silicon, enabling seamless mode switching and versatile wavefront manipulation. By leveraging the photo-induced dielectric-to-metallic transition, the device functions as a high-efficiency transmission-type polarization converter under zero pump fluence, transforming incident *X*-polarized waves into *Y*-polarized waves across a broad frequency range of 0.85–1.5 THz, with a polarization conversion ratio (PCR) exceeding 99%. Upon excitation by 800 nm near-infrared laser pulses, the metasurface transitions to reflection mode, where it simultaneously achieves linear polarization conversion and generates dual-channel orbital angular momentum (OAM) beams through a phase-coding strategy integrated with Fourier convolution. Furthermore, by employing the Gerchberg–Saxton (GS) algorithm to optimize the phase profile, holographic reconstruction is realized in the far field. This design integrates diverse manipulation capabilities into a single, dynamically controllable platform, offering a promising technological approach for THz information processing and integrated photonic systems.

Keywords: terahertz; metasurface; photosensitive silicon; polarization conversion; orbital angular momentum; hologram

1. Introduction

Terahertz (THz) waves possess unique characteristics—including high penetrability, high frequency, and non-ionizing safety—that enable transformative applications in wireless communication, biomedical imaging, and sensing [1–4]. To achieve efficient manipulation and multidimensional control of these waves, metasurfaces have emerged as a pivotal technology. By precisely engineering sub-wavelength microstructures, metasurfaces allow for flexible control over THz amplitude, phase, and polarization. Their ultrathin profile and high design flexibility have led to superior performance in diverse fields, such as electromagnetic cloaking [5,6], THz lenses [7,8], and advanced beam shapers [9–11].

Despite their prowess in wavefront control, most terahertz metasurfaces remain constrained by static, single-function designs that fail to meet the requirements of multifunctional integrated systems. This limitation has driven the development of dynamic

Received: 23 April 2026
Revised: 14 May 2026
Accepted: 26 May 2026
Published: 2 June 2026

platforms; notably, coding metasurfaces [12,13] and those incorporating tunable materials such as graphene [14–17], liquid crystals [18,19], or phase-change materials [20–22]. Among these, photosensitive silicon [23–25] has emerged as a particularly promising candidate for reconfigurable devices, enabling agile electromagnetic modulation through optically controlled conductivity.

Recent advancements in photosensitive silicon-based metasurfaces have transitioned from fundamental parameter modulation to sophisticated, multidimensional wavefront engineering. Research has evolved from platforms capable of basic concurrent regulation of amplitude, phase, and polarization to complex hybrid architectures [26]. By integrating photosensitive silicon with other functional materials such as graphene or gold, researchers have demonstrated diverse capabilities, including broadband absorption, circular dichroism, and dynamic vortex beam generation via Pancharatnam–Berry (PB) phase modulation [27]. These hybrid designs allow for high-purity multimodal beam steering and polarization imaging without requiring structural geometry modifications, significantly enhancing the versatility of optically tunable devices [28]. Nevertheless, achieving localized, high-precision control over phase distribution remains a persistent challenge, which continues to limit the full potential of complex terahertz wave manipulation.

In this paper, we propose a transmissive–reflective tunable coding metasurface based on photosensitive silicon. Different from conventional static designs, our proposed structure exploits the optical-pump-dependent conductivity of silicon to dynamically switch between transmission and reflection operating modes. Specifically, we demonstrate that the device functions as a high-efficiency polarization converter in the transmission regime. Upon switching to the reflection regime, it sustains the capability of linear polarization conversion while simultaneously serving as a multifunctional wavefront modulator for OAM beam generation and holographic imaging. This work provides a versatile strategy for active terahertz wave manipulation, offering a viable route for reconfigurable communication and imaging systems.

2. Design of Metasurface Unit Cells

As illustrated in Figure 1a, the proposed metasurface unit cell adopts a tri-layer sandwich structure with a periodicity of P. The top layer consists of a wrench-shaped copper (Cu) resonator, characterized by a thickness of h_2, a circular radius of d, and a connecting arm length of l. The copper material is modeled with an electrical conductivity of $\sigma = 5.8 \times 10^7$ S·m^{-1}. To introduce additional phase control, the orientation of the resonator is defined by a rotation angle α in Figure 1b. The intermediate spacer is composed of a polyimide dielectric layer with a thickness of h_1, a relative permittivity of 3.5, and a loss tangent of 0.0027. The bottom layer features an alternating arrangement of photosensitive silicon and copper grids, with a uniform thickness of h_2 and strip widths defined as w_1, w_2, and w_3, respectively. The optimized geometric parameters are $P = 100$ µm, $h_1 = 30$ µm, $r = 15$ µm, $d = 8$ µm, $l = 20$ µm, $h_2 = 1$ µm, $h_3 = 1$ µm, $w_1 = 12$ µm, $w_2 = 8$ µm, and $w_3 = 4$ µm. Unit cell simulations in CST utilized xy-periodic and z-open boundaries to model the infinite array response.

To justify the selected geometric parameters and optimize the device performance, a parametric sweep was conducted for key dimensions, as shown in Figure 2. The dielectric thickness h_1 and outer radius r primarily determine the phase matching and resonance frequencies. Varying these parameters reveals that $h_1 = 30$ µm and $r = 15$ µm provide the most stable PCR across the 0.8 to 1.6 THz band. The internal parameter d is particularly critical for balancing the operating bandwidth and in-band flatness; while smaller values yield a narrower bandwidth, larger values introduce a noticeable PCR dip near 1.25 THz. Optimizing this parameter to $d = 8$ µm effectively broadens the high-efficiency bandwidth

without causing mid-band degradation. Finally, the wire width $w_1 = 12$ μm was selected to balance high-frequency stability and manufacturing tolerance. Collectively, this optimized configuration ensures near-unity conversion efficiency over the target terahertz spectrum.

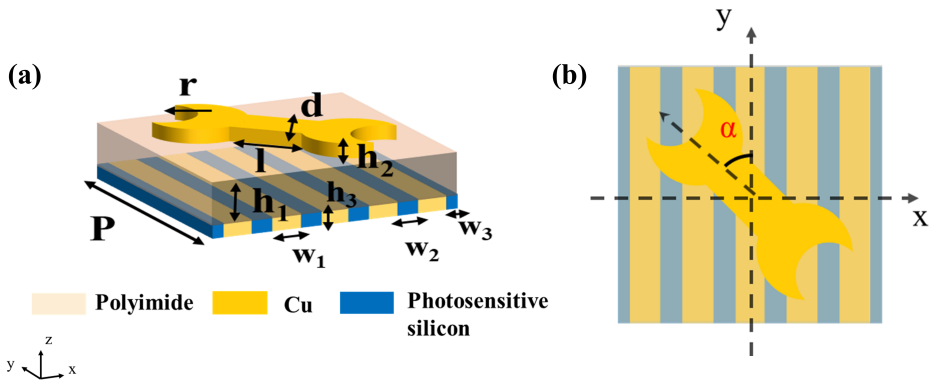

Figure 1. (**a**) Metasurface unit structure. (**b**) Top view of unit structure.

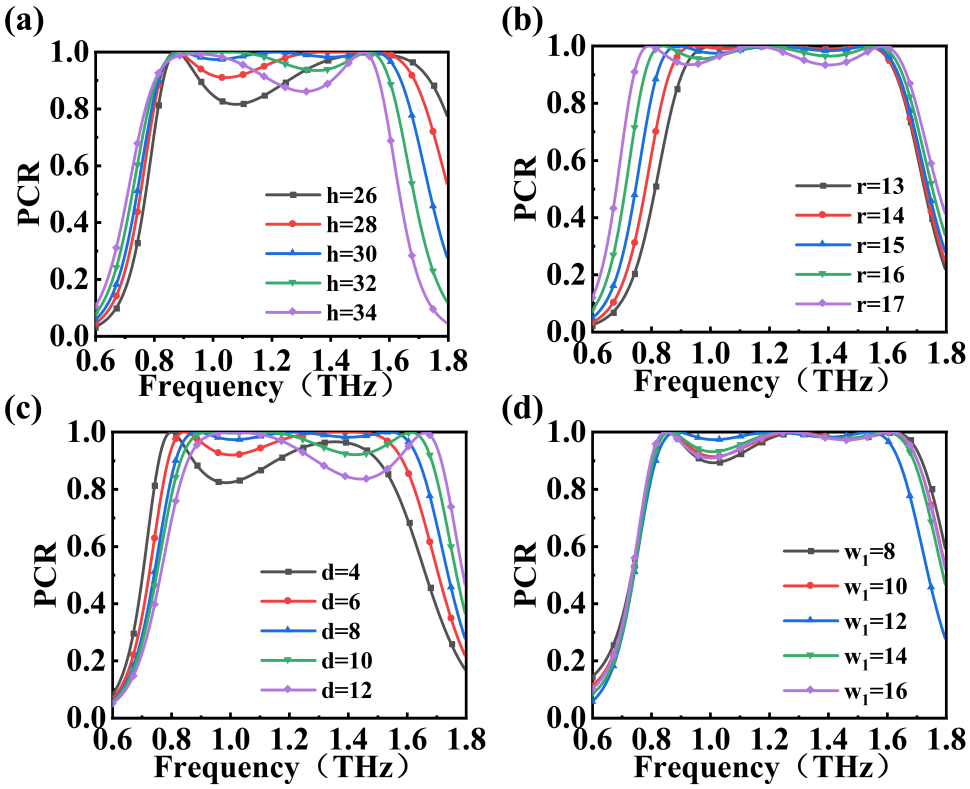

Figure 2. The influence of the parameters of the super-surface unit part on the polarization conversion rate (**a**) h; (**b**) r; (**c**) d; (**d**) w_1.

Photosensitive silicon is particularly suitable for tunable metasurfaces due to its light-dependent electrical properties, with a relative permittivity of 11.7. A near-infrared laser pulse with a central wavelength of 800 nm is employed as the optical pump to excite carriers in the silicon. The conductivity of photosensitive silicon is governed by the pump fluence, and its tunable behavior under optical excitation is modeled accordingly. The relationship between the conductivity of photosensitive silicon and the pump fluence is expressed as [29]

$$\sigma_{\mathrm{Si}}(I) = 4.863 \times 10^{-4} I^2 + 0.1856 I + 1.569 \quad (1)$$

where σ_{Si} denotes the conductivity (S/m), and I represents the pump fluence (mJ/cm^2). Based on this equation, the conductivity of photosensitive silicon is designed for different

pump fluences. In the absence of optical pumping (pump fluence = 0), the conductivity of silicon is set to 1 S/m, whereas under excitation by a near-infrared laser pulse with a central wavelength of 800 nm (pump fluence = 294.6 μJ/cm^2), the conductivity reaches 10^5 S/m. Using this characteristic, the metasurface unit can realize dynamic switching between the transmission mode and the reflection mode. The equivalent diagram of the working principle is shown in Figure 3, so as to realize diversified electromagnetic response control.

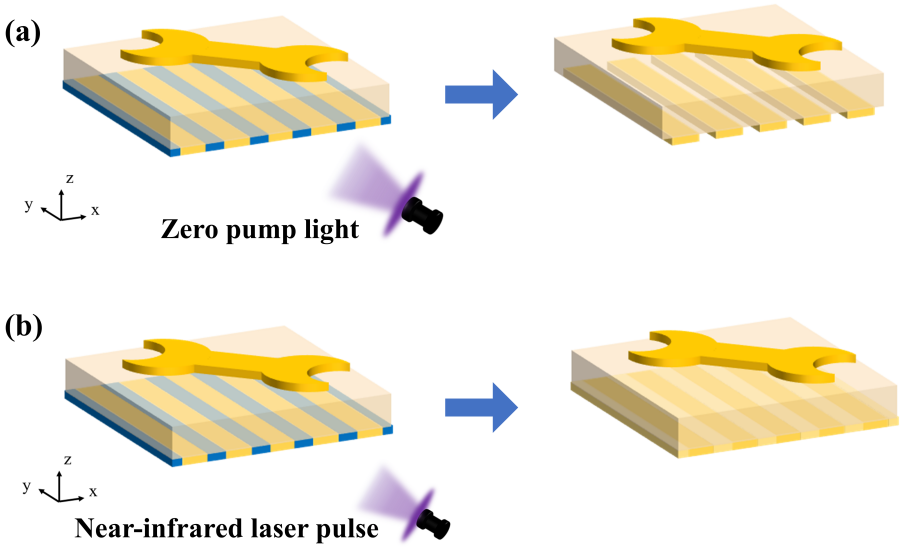

Figure 3. The equivalent diagram of the metasurface structure under different excitation conditions. (**a**) When the pump flux is zero, the metasurface unit exhibits a transmission mode. (**b**) When the near-infrared laser pulse is excited, the metasurface unit is in reflection mode.

To realize the desired polarization conversion and phase modulation, the polarization response of our metasurface is rigorously described using the Jones matrix formalism. Leveraging the Pancharatnam–Berry (P-B) phase principle, precise wavefront manipulation is achieved by spatially rotating the orientation of the anisotropic meta-atoms. In the local principal axes (x', y') of the anisotropic meta-atom, the Jones matrix can be expressed as [30]

$$J_0 = \begin{bmatrix} e^{i\varphi_x} & 0 \\ 0 & e^{i\varphi_y} \end{bmatrix}, \tag{2}$$

where φ_x and φ_y denote the phase delays along the two principal axes. When the element is rotated by an angle α with respect to the global (x, y) coordinates, the effective Jones matrix becomes

$$J' = \Re(-\alpha)\, J_0\, \Re(\alpha), \qquad \Re(\alpha) = \begin{bmatrix} \cos\alpha & -\sin\alpha \\ \sin\alpha & \cos\alpha \end{bmatrix}. \tag{3}$$

After expansion, one obtains

$$J' = \begin{bmatrix} c^2 e^{i\varphi_x} + s^2 e^{i\varphi_y} & cs\,(e^{i\varphi_y} - e^{i\varphi_x}) \\ cs\,(e^{i\varphi_y} - e^{i\varphi_x}) & s^2 e^{i\varphi_x} + c^2 e^{i\varphi_y} \end{bmatrix}, \tag{4}$$

with $c = \cos\alpha$ and $s = \sin\alpha$. By introducing the average phase $\mu = (\varphi_x + \varphi_y)/2$ and the half-difference $\Delta = (\varphi_x - \varphi_y)/2$, the compact form is

$$J' = e^{i\mu} \begin{bmatrix} \cos\Delta + i\cos 2\alpha \sin\Delta & -i\sin\Delta\sin 2\alpha \\ -i\sin\Delta\sin 2\alpha & \cos\Delta - i\cos 2\alpha\sin\Delta \end{bmatrix}. \tag{5}$$

In the transmission mode, we consider an *X*-polarized input

$$\mathbf{E}_{\text{in}} = \begin{bmatrix} 1 \\ 0 \end{bmatrix}, \qquad \mathbf{E}_{\text{out}} = J'\mathbf{E}_{\text{in}} = \begin{bmatrix} J'_{11} \\ J'_{21} \end{bmatrix}, \tag{6}$$

where the output consists of a co-polarized term ($E_x = J'_{11}$) and a cross-polarized term ($E_y = J'_{21}$). Efficient polarization rotation from *X*-polarization to *Y*-polarization is achieved when $|J'_{21}|$ is maximized while $|J'_{11}|$ is minimized, which is the primary function of the metasurface in transmission. In the reflection mode, we consider circularly polarized incidence, with Jones vectors defined as [31]

$$E_{\text{RCP}} = \tfrac{1}{\sqrt{2}} \begin{bmatrix} 1 \\ -i \end{bmatrix}, \qquad E_{\text{LCP}} = \tfrac{1}{\sqrt{2}} \begin{bmatrix} 1 \\ i \end{bmatrix}. \tag{7}$$

When the condition $\varphi_x - \varphi_y = \pi$ is satisfied, an incident RCP wave is completely converted into an LCP wave with an additional phase factor:

$$E_{\text{out}} = e^{i2\alpha} e^{i\mu} \frac{1}{\sqrt{2}} \begin{pmatrix} \cos\Delta + \sin\Delta \\ -i(\cos\Delta + \sin\Delta) \end{pmatrix} = e^{i2\alpha} E_{\text{LCP}} \tag{8}$$

The additional phase -2α corresponds to the Pancharatnam–Berry (PB) geometric phase, which arises solely from the in-plane rotation of the anisotropic element. By tailoring the spatial distribution of the rotation angle $\alpha(\mathbf{r})$, a desired PB phase profile $\Phi_{\text{PB}}(\mathbf{r}) = -2\alpha(\mathbf{r})$ can be encoded onto the reflected wavefront, thereby enabling vortex beam generation and holographic image reconstruction.

3. Results and Discussion

3.1. Linear Polarization Converter

Under zero pump fluence, the electrical conductivity of the photosensitive silicon drops to 1 S/m, rendering it a dielectric. Consequently, the bottom copper layer dominates the electromagnetic response, allowing the metasurface to operate in transmission mode, as shown in Figure 4a. Within the frequency-domain solver's boundary configurations, the scatterer is defined by periodic unit cell boundary conditions along the *x* and *y* axes, while Floquet ports are employed in the longitudinal direction to extract the simulation data. In this state, an incident X-polarized wave propagates through the intermediate dielectric layer and the grating structure. When the unit cell is oriented at 45°, the incident wave is efficiently converted into a high-purity Y-polarized wave. Conversely, under excitation by a near-infrared laser pulse with a central wavelength of 800 nm, the conductivity reaches 10^5 S/m. Driven by this metallic behavior, the metasurface switches to reflection mode. Remarkably, maintaining the same 45° orientation, the unit cell continues to function as an efficient linear polarization converter for the reflected wave, as depicted in Figure 4d.

To evaluate the linear polarization regulation ability of the designed polarization conversion metasurface, the PCR is introduced as a performance index [32]:

$$\text{PCR} = \frac{|T_{yx}|^2}{|T_{yx}|^2 + |T_{xx}|^2} = \frac{|R_{yx}|^2}{|R_{yx}|^2 + |R_{xx}|^2} \tag{9}$$

where T_{xx} and T_{yx} represent the co-polarized and cross-polarized transmission coefficients, respectively, while R_{xx} and R_{yx} denote the corresponding reflection coefficients. The PCR value approaching unity indicates that the incident energy is predominantly converted into the orthogonal polarization state, demonstrating high-efficiency polarization conversion.

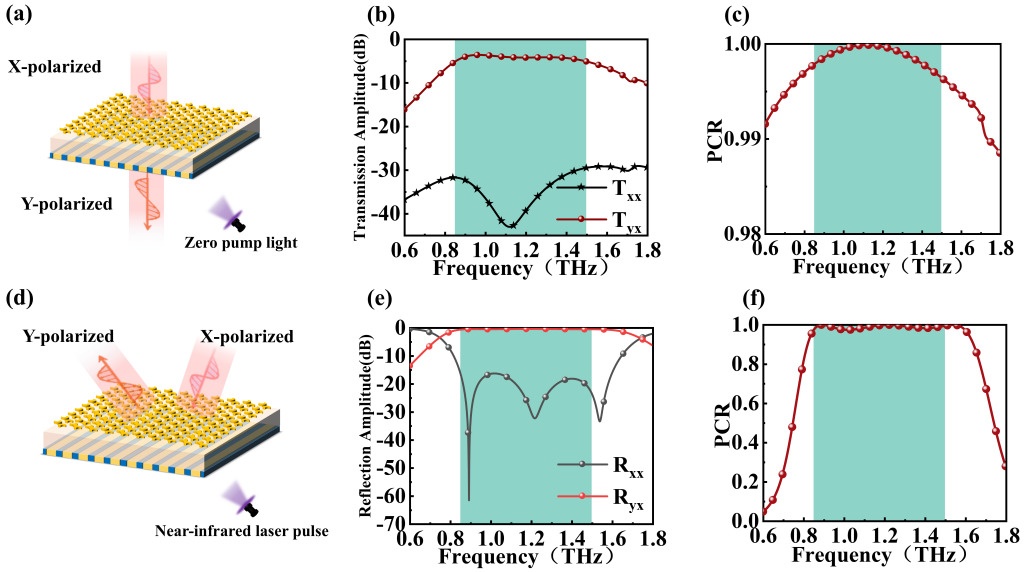

Figure 4. Simulation results of linear polarization conversion. (**a**–**c**) Transmission mode: schematic diagram, transmission spectra, and PCR. (**d**–**f**) Reflection mode: schematic diagram, reflection spectra, and PCR.

The transmission characteristics are illustrated in Figure 4b. The cross-polarized transmission coefficient (T_{yx}) maintains a level above −5 dB across a broad frequency range from 0.85 THz to 1.5 THz, while the co-polarized component (T_{xx}) remains suppressed below −30 dB throughout the same band. As shown in Figure 4c, the PCR exceeds 99.8% within this range, indicating that the vast majority of the transmitted power is coupled into the cross-polarization channel. As shown in Figure 4e, the cross-polarization reflection coefficient (R_{yx}) approaches 0 dB across 0.85–1.5 THz, yielding PCR exceeding 90% in Figure 4f. The result demonstrates that the proposed metasurfaces function as a broadband and high-efficiency linear polarization converter, exhibiting excellent performance in both transmission and reflection modes.

3.2. Dual-Channel OAM Vortex Beam

Under excitation by a near-infrared laser pulse with a central wavelength of 800 nm, the electrical conductivity of the photosensitive silicon (σ_{Si}) reaches 10^5 S/m, inducing a metallic state. In this mode, the photosensitive silicon and the underlying copper grid collaboratively form an effective reflective ground plane, causing the metasurface to operate in reflection mode. As illustrated in Figure 5, based on the geometric phase principle, eight unit cells are selected with rotation angles ranging from 0° to 157.5° at an incremental step of 22.5°. This configuration establishes a constant phase gradient with a 45° phase progression between adjacent units, thereby achieving full 360° phase coverage across the eight-unit sequence.

Full-wave electromagnetic simulations were performed using CST to evaluate the reflective performance of the designed unit, as illustrated in Figure 6a. Under circularly polarized wave incidence, the amplitude of the cross-polarized reflection component remains close to 1 across the entire operating band, indicating nearly perfect reflection efficiency (Figure 6b). To investigate the PB phase modulation, the phase responses of meta-atoms with varying rotation angles α were analyzed for both left-handed circularly polarized (LCP) and right-handed circularly polarized (RCP) waves. As shown in Figure 6c, the induced phase shifts for LCP and RCP incidences exhibit linear relationships with opposite gradients ($\pm 2\alpha$), which is fully consistent with geometric phase theory. Furthermore, the polarization conversion rates for various α values are presented in Figure 6d. The PCR remains above

0.9 across the 0.8–1.6 THz range for all rotation angles, providing further validation of the metasurface's high-efficiency polarization conversion capabilities in reflection mode.

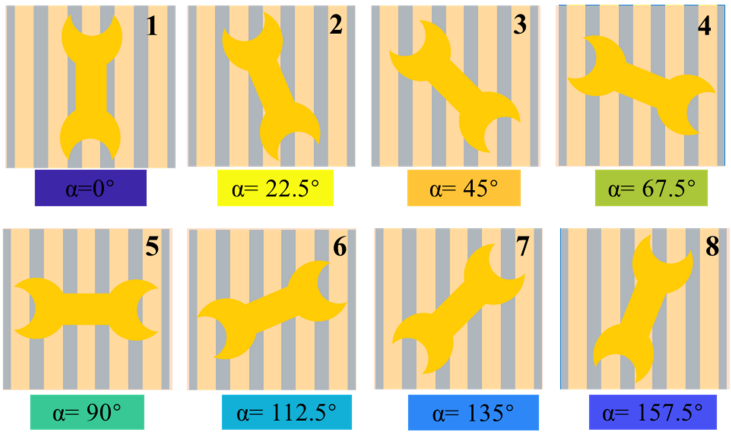

Figure 5. Eight metasurface unit cells with different rotation angles α.

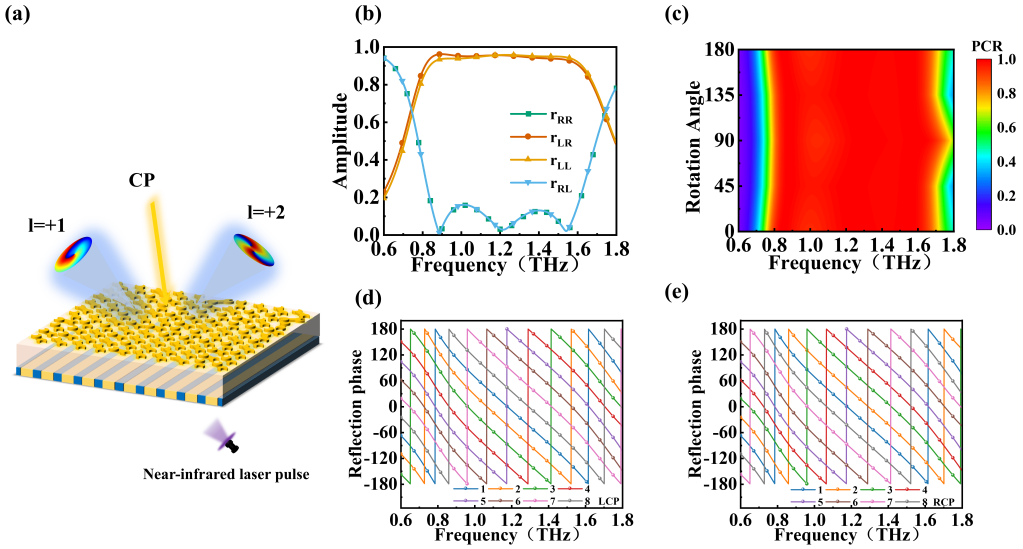

Figure 6. Simulation of OAM generation and reflection properties. (**a**) Schematic of dual-channel OAM generation. (**b**) Simulated reflection amplitudes. (**c**) PCR distribution map versus frequency and rotation angle. (**d**,**e**) Reflection phase spectra under LCP and RCP incidence.

The vortex beam is characterized by a distinctive annular intensity distribution and a helical phase profile. Owing to the OAM it carries and its theoretically unbounded topological charge, the vortex beam introduces an additional degree of freedom for photon information encoding, thereby significantly enhancing the channel capacity of communication systems without requiring increased bandwidth. As a result, vortex beams have attracted widespread interest for their promising applications in advanced fields such as wavefront manipulation, target detection, and terahertz imaging. The design of a metasurface array capable of generating vortex beams needs to take into account the energy loss of each metasurface element under incident excitation. Therefore, each element must be calculated using the phase compensation formula to obtain the required phase correction. The phase compensation formula is expressed as follows [33]:

$$\varphi(x, y) = l \cdot \arctan\left(\frac{x}{y}\right) \tag{10}$$

Here, (x, y) represents the central coordinates of each metasurface element, and l is the topological charge number of the vortex beam. According to the reflection phase provided by each metasurface unit, the elements are arranged to form a specific wavefront. For the array with a topological charge of $l = +1$, the phase of the unit cells varies by 2π when rotating one full circle around the coordinate center. Similarly, for the array with a topological charge of $l = +2$, the phase varies by $2 \times 2\pi$ along a complete rotation around the center, as illustrated in Figure 7.

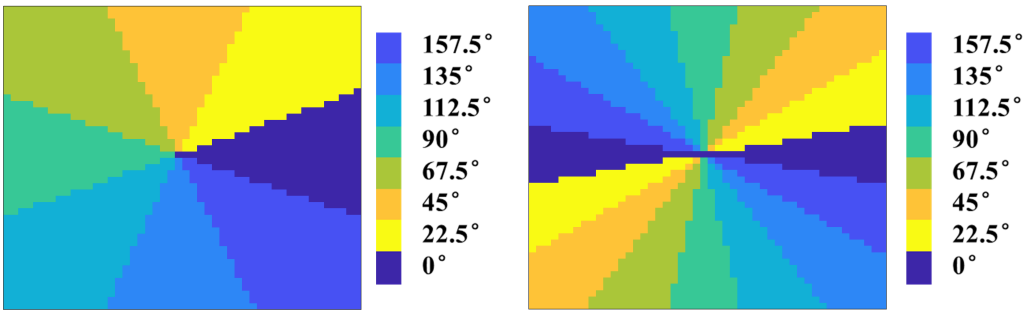

Figure 7. Compensated phase distributions for $l = +1$ and $l = +2$.

To verify the capability of the proposed metasurface in generating OAM beams, full-wave simulations were performed for target topological charges of $l = 1$ and $l = 2$. Figure 8 presents the simulated electric field distributions and mode purity analysis for these configurations. As observed in Figure 8a,d, the amplitude profiles exhibit the characteristic doughnut-shaped intensity distributions with distinct central phase singularities, where the field intensity vanishes. Notably, the radius of the central dark core expands as the topological charge increases from 1 to 2, consistent with the theoretical properties of vortex beams. The corresponding phase distributions, illustrated in Figure 8b,e, reveal clear spiral phase wavefronts carrying the orbital angular momentum. Specifically, the $l = 1$ mode undergoes a continuous 2π phase variation around the center, while the $l = 2$ mode displays two intertwined spiral arms with a total phase accumulation of 4π, confirming the precise imprint of the desired azimuthal phase gradients. To quantitatively evaluate the beam quality, the purity of OAM was calculated using spectral analysis [34].

$$A_l = \frac{1}{2\pi} \int_0^{2\pi} \psi(\varphi) \cdot e^{-jl\varphi} d\varphi \tag{11}$$

$$\psi(\varphi) = \sum_{l=-\infty}^{+\infty} A_l \cdot e^{jl\varphi} \tag{12}$$

$$\text{Purity} = \frac{|A_l|^2}{\sum_{l'=-\infty}^{+\infty} |A_{l'}|^2} \tag{13}$$

Here, A_ℓ represents the modal amplitude, and $\psi(\varphi)$ represents the sampled complex electric field distribution. The purity of the OAM vortex is expressed by calculating the ratio of the target modal energy to the total radiated energy. As shown in Figure 8c and Figure 8f, the energy is highly concentrated in the target modes, with purities reaching approximately 86% and 87% for the $l = 1$ and $l = 2$ states, respectively. These results demonstrate the high-fidelity wavefront manipulation capability of the designed metasurface.

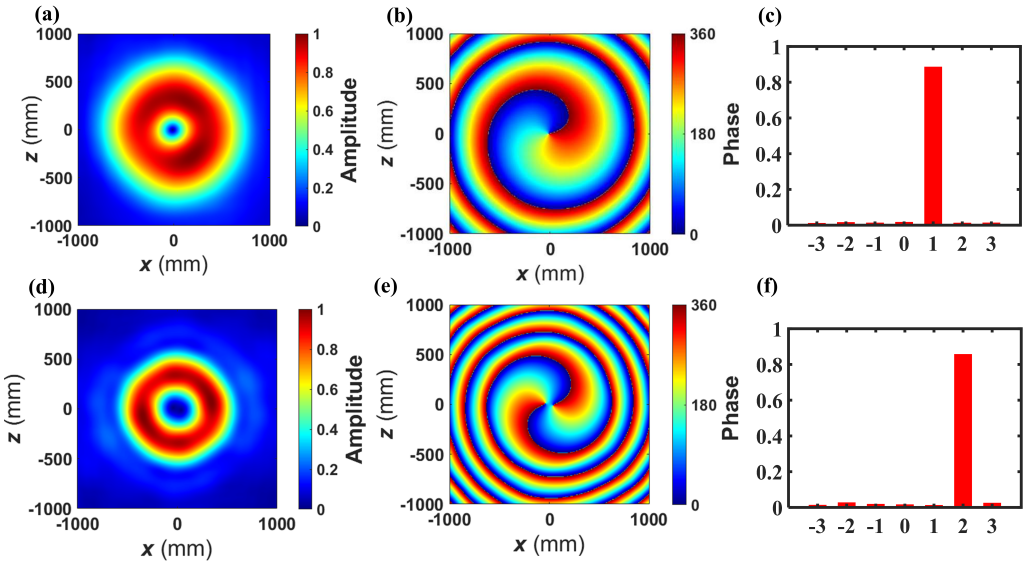

Figure 8. Simulated field distributions and mode purity analysis of the generated OAM beams. (**a**–**c**) The normalized amplitude distribution, phase distribution, and mode purity spectrum for the OAM beam with a topological charge of $l = +1$. (**d**–**f**) The normalized amplitude distribution, phase distribution, and mode purity spectrum for the OAM beam with a topological charge of $l = +2$.

To achieve flexible control over the radiation direction of vortex beams, metasurfaces can impose new modulation sequences on existing phase codes by leveraging the convolution principle of far-field radiation patterns. Based on the Fourier transform framework, a specially designed vortex metasurface structure is proposed, wherein the deflection of the emitted vortex beam is realized through the convolution theorem. This enables directional control of the beam propagation while preserving its OAM characteristics. To provide a more intuitive understanding of the physical basis of the convolution operation, it can be analogized to the modulation process in signal processing: the multiplication of two signals in the time domain corresponds to the convolution of their spectra in the frequency domain. The detailed numerical relationship can be expressed as [35]

$$w(t) = u(t) \cdot v(t) \overset{\text{FT}}{\Leftrightarrow} W(\omega) = U(\omega) * V(\omega) \tag{14}$$

Here, t represents the time-domain signal and ω represents the frequency-domain signal. According to the convolution theorem, the convolution integral of two signals in the time domain corresponds to the product of the Fourier transforms of the two signals in the frequency domain. Specifically, when the encoding sequence is regarded as the time domain, the far-field pattern is regarded as the frequency domain and is represented as

$$w(x) = u(x) \cdot v(x) \Leftrightarrow W(\sin\theta) = U(\sin\theta) * V(\sin\theta) \tag{15}$$

Among them, x is the relative dimension of the metasurface component at the response frequency, and θ is the direction angle of the far-field beam. Suppose in Equation (11), $V(\omega)$ is the impulse function $\delta(t)$, and when the impulse function moves ω_0 towards the central frequency, $\sigma(\omega - \omega_0)$ in the frequency domain and is expressed in the time domain as $e^{j\omega_0 t}$. Similarly, $e^{j \sin\theta_0 x}$ in the encoded metasurface, and the phase gradient is expressed as the pulse function moving θ_0 in the frequency domain. Therefore, Equation (12) can be written as

$$w(x) = u(x) \cdot e^{j \sin\theta_0 x} \Leftrightarrow W(\sin\theta) = U(\sin\theta) * \sigma(\sin\theta - \sin\theta_0) \tag{16}$$

This formula characterizes the amplitude and gradient phase distribution of the metasurface. By leveraging the convolution theorem in conjunction with PB phase and segmentation compensation strategies, the superposition of coding sequences in the spatial domain is mapped onto the convolution of the far-field scattering pattern. Consequently, by superimposing an initial vortex phase with a specific phase gradient sequence, the generated OAM beam can be spatially steered to a desired orientation. Specifically, when a vortex OAM sequence with $l = +1$ is superimposed with first- and second-level coding sequences corresponding to "up" and "right" phase gradients, respectively, the resulting $+1$ OAM beam is directed to the upper-right quadrant. Similarly, combining an $l = +2$ OAM mode with "lower" and "left" coding sequences steers the $+2$ OAM beam to the lower-left position. The schematic representation of this phase superposition and convolution process is illustrated in Figure 9.

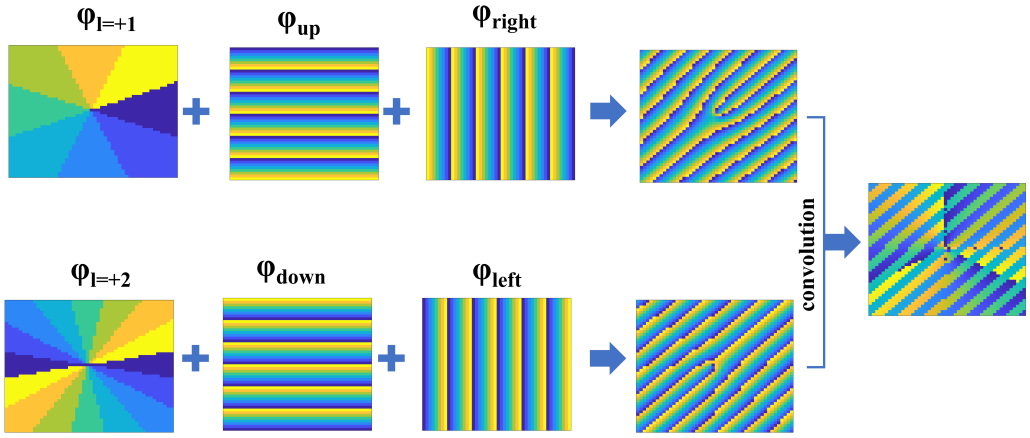

Figure 9. Schematic of the convolution coding principle. Synthesis of the final dual-channel coding pattern by superposing vortex and gradient phases followed by a convolution operation.

The resulting phase pattern is numerically simulated to visualize the spatial electric field distribution, as shown in Figure 10a. The reflected electric field vector distribution, which simultaneously generates OAM beams with $l = +1$ and $l = +2$, is illustrated in Figure 10b. It is clearly observed that an OAM beam with a topological charge of $+1$ is formed in the upper-right quadrant, while an $l = +2$ beam emerges in the lower-left quadrant. The corresponding far-field intensity pattern shown in Figure 10c further confirms this observation, exhibiting excellent agreement with the near-field electric field vector distribution.

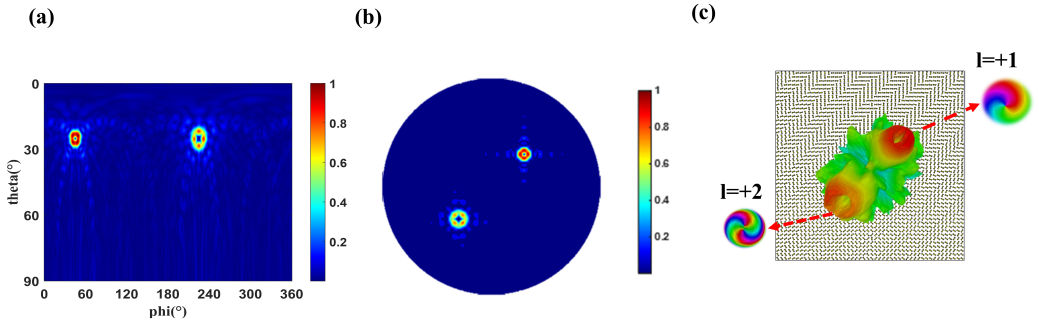

Figure 10. (**a**) Electric field azimuth diagram. (**b**) Dual-beam electric field vector diagram. (**c**) Far-field simulation diagram.

3.3. Metasurface Holographic Imaging

Based on the previously designed metasurface unit, the application in holographic imaging is further demonstrated. In order to obtain the corresponding phase distribution

of the target image, the Gerchberg–Saxton algorithm is used [36]. The iterative algorithm reconstructs the phase information based on the amplitude and partial phase of the known target and generates a phase-only hologram that can produce the required diffraction and imaging effects. By alternately performing Fourier transform and inverse Fourier transform between spatial domain and frequency domain, the GS algorithm converges to a phase matrix suitable for holographic coding. The flow diagram of the GS algorithm is shown in Figure 11:

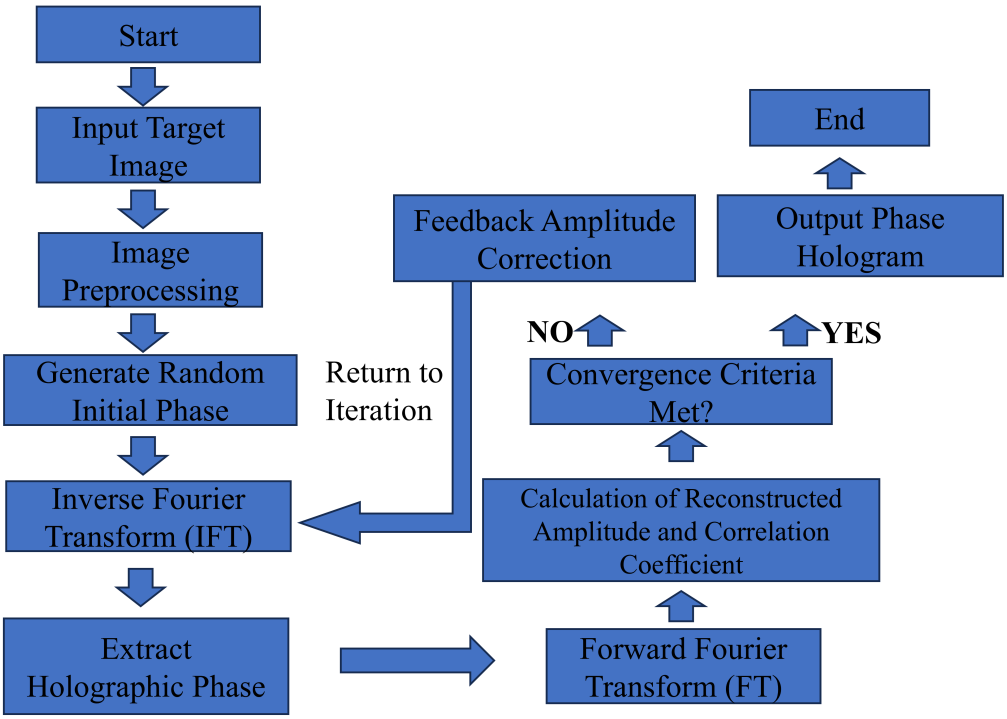

Figure 11. GS algorithm flow diagram.

The target image is set as the graphical representation of the letters "QDU" in Figure 12a. The discretized phase profile obtained through the GS algorithm is shown in Figure 12b. The specific arrangement of the superstructure units is shown in Figure 12c. In the reflective mode under Gaussian polarization wave illumination along the z-axis within the 1.2–1.3 THz frequency range, the electric field distribution was acquired. The far-field holographic image reconstructed from the post-processed simulated electric field data is presented in Figure 12d. To quantitatively define the operational bandwidth, the image fidelity is evaluated using the two-dimensional Pearson Correlation Coefficient (PCC) [37].

$$\mathrm{PCC} = \frac{\sum_m \sum_n (I_{sim}(m,n) - \bar{I}_{sim})(I_{ref}(m,n) - \bar{I}_{ref})}{\sqrt{(\sum_m \sum_n (I_{sim}(m,n) - \bar{I}_{sim})^2)\left(\sum_m \sum_n (I_{ref}(m,n) - \bar{I}_{ref})^2\right)}} \quad (17)$$

where $I_{sim}(m,n)$ represents the normalized intensity of the reconstructed holographic image at a given frequency, and $I_{ref}(m,n)$ is the spatial intensity of the ideal reference target. $\bar{I}_{sim}$ and $\bar{I}_{ref}$ denote their respective mean values across the entire two-dimensional spatial domain. The fidelity peaks at 0.5992 at the central frequency of 1.25 THz and slightly decreases to 0.5606 and 0.5874 at 1.2 THz and 1.3 THz, respectively. This decrease, attributed to dispersion and phase quantization errors, mathematically explains the visually fainter images at the band edges. Nevertheless, the fidelity remains robustly above 0.55, demonstrating a stable effective holographic bandwidth across 1.2–1.3 THz.

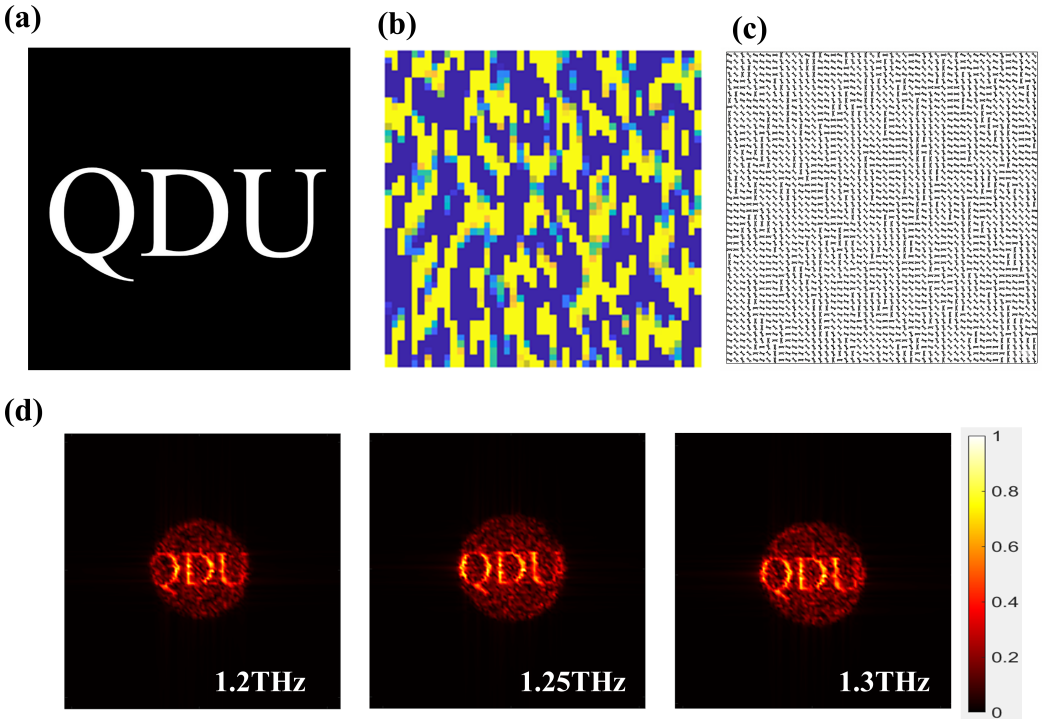

Figure 12. (**a**) Target image. (**b**) Holographic phase obtained by using the GS algorithm. (**c**) Arrangement of metasurface units. (**d**) Reconstructed hologram from simulated electric field.

3.4. Potential Metasurface Manufacturing and Experimental Testing

Experimental implementation and sample fabrication are crucial for validating the performance of the designed metasurface model. Although this study primarily focuses on numerical simulations, we propose a potential metasurface fabrication process, as illustrated in Figure 13. The silicon substrate is initially ultrasonically cleaned with acetone, ethanol, and deionized water, and then dried with nitrogen gas. A copper thin film is deposited via sputtering, followed by photolithography to define the underlying metal strip grating structure. A photosensitive silicon film is subsequently deposited on the sample surface using plasma-enhanced chemical vapor deposition (PECVD), and patterned into alternating strip structures with the copper layer through photolithography and reactive ion etching. A polyimide (PI) film is then spin-coated over the structured surface and gradually cured under a nitrogen atmosphere to form a uniform dielectric layer. Another copper thin film is deposited on top of the PI layer, and photolithography is employed to define the desired metasurface unit pattern, yielding the top-layer wrench-shaped structures. This completes the fabrication process of the metasurface device [38].

The experimental setups under two operating conditions are illustrated in Figure 14. Common components used in both configurations include a terahertz detector, a terahertz probe, and optical lenses. In the reflection mode, as shown in Figure 14a, a right-handed circular polarizer is employed to convert the emitted terahertz wave into right-handed circularly polarized radiation. In the transmission mode, as depicted in Figure 14b, a linear polarizer is used to convert the terahertz wave into X-polarized radiation. By placing the metasurface at different testing positions, the final results are recorded by the terahertz detector [39].

Table 1 provides a comprehensive comparison between the proposed metasurface and other representative works in the literature. By evaluating key metrics such as working mode, material, operating frequency, and realization function, it is evident that work possesses a significant comparative advantage. Specifically, unlike most existing designs, the proposed metasurface achieves dynamic switching between reflection and transmis-

sion modes while simultaneously supporting three distinct electromagnetic functions. This versatility underscores the superiority of our approach in multifunctional terahertz wave manipulation.

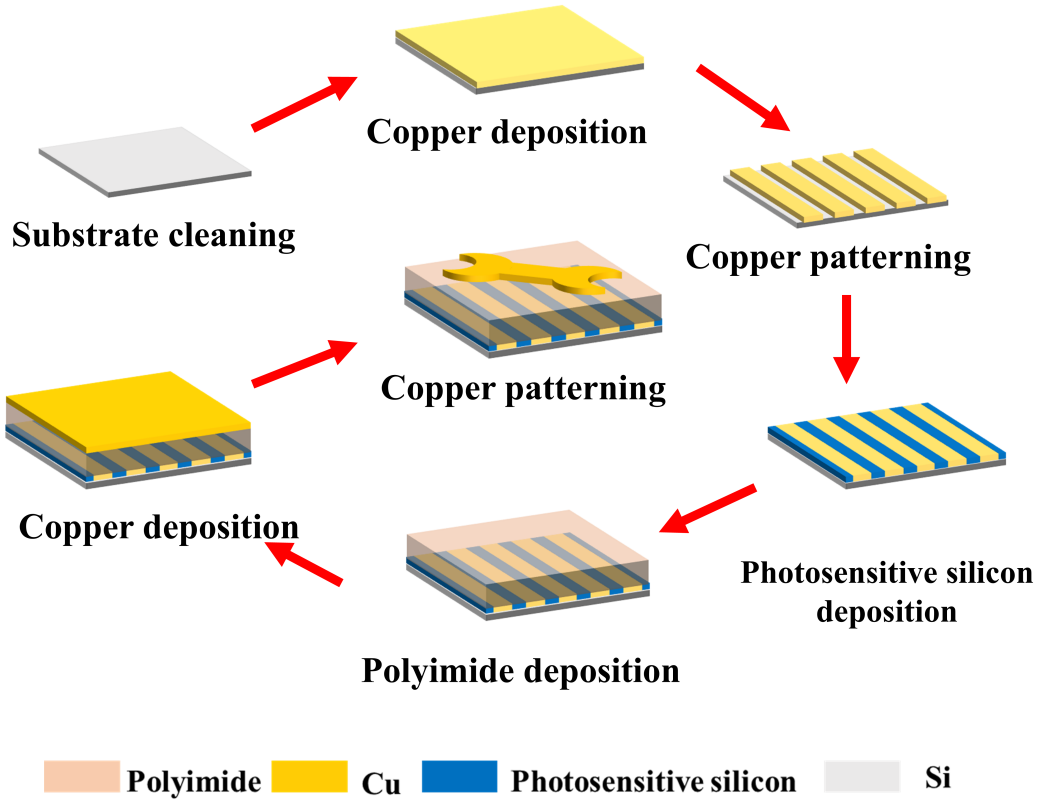

Figure 13. Fabrication process of tunable terahertz metasurface based on photosensitive silicon.

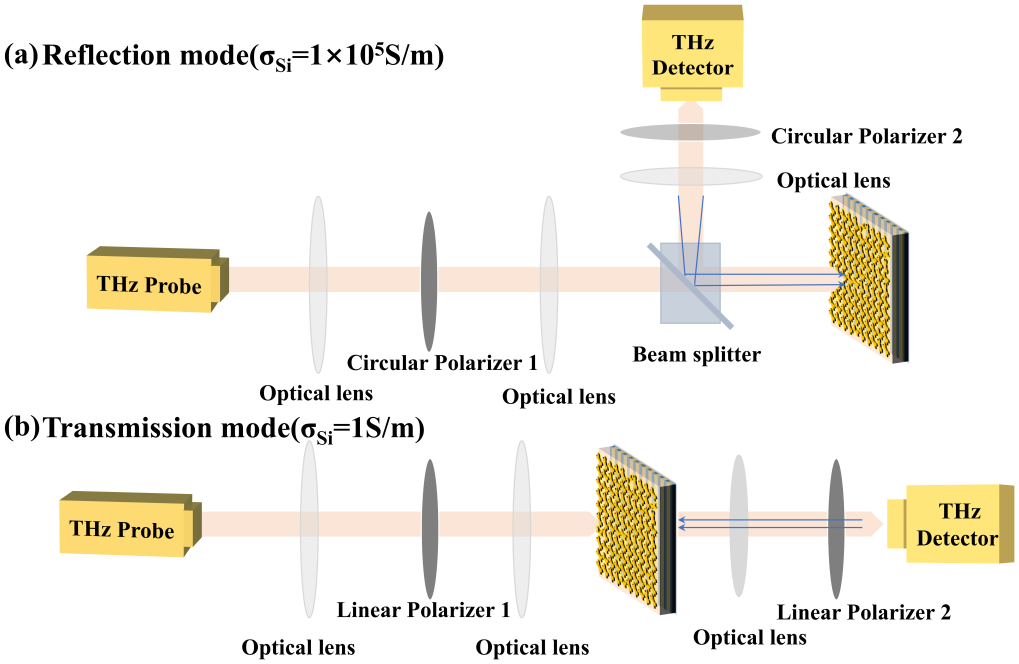

Figure 14. (**a**) Schematic of the experimental setup in reflection mode. (**b**) Schematic of the experimental setup in transmission mode.

Table 1. Metasurface performance comparison table.

Literature	Working Mode	Material	Operating Frequency	Realization Function
[40]	Reflection	VO_2 graphene	0.8–2.2 THz	Absorption Beam Steering
[41]	Reflection	VO_2	0.5–2.0 THz	OAM Order Switching
[42]	Reflection	VO_2	0–2.0 THz	Independent Amplitude-Phase Modulation
[43]	Reflection	Photosensitive silicon	0.6–1.3 THz	Spin-Decoupled Logic Holography
This work	Reflection Transmission	Photosensitive silicon	0.6–1.8 THz	Polarization Converter Dual-Channel OAM Beam Holographic Imaging

4. Conclusions

In conclusion, this paper designs a tunable coding metasurface with controllable light intensity. Under zero pump fluence conditions, the metasurface exhibits a transmission mode. The incident X-polarized terahertz wave can achieve broadband and efficient linear polarization conversion in the 0.85–1.5 THz band, and the PCR is greater than 99%, indicating that the designed unit has good polarization control ability in the transmission state. Upon excitation by near-infrared laser pulses with a central wavelength of 800 nm, the metasurface exhibits a reflection mode. In this state, the metasurface can not only achieve linear polarization conversion in the 0.85–1.5 THz band, and the PCR is greater than 90%, but also, it can be used for more complex wavefront control. Based on the phase control ability in the reflection mode and the principle of Fourier convolution, a dual-channel OAM vortex beam coding array is constructed, and the dual-channel OAM vortex beams with topological charges of l = +1 and l = +2 are realized. The GS algorithm is used to obtain the discrete phase distribution required for the target image holography, and the far-field holographic reconstruction of the target image is realized in the 1.2–1.3 THz band. It has certain application prospects in terahertz dynamic wavefront control, information communication, and holographic display.

Author Contributions: Conceptualization, Z.L. and P.X.; methodology, Z.L.; software, Z.L.; validation, H.Z. and T.L.; formal analysis, Z.L. and H.Z.; investigation, Z.L. and P.X.; resources, Z.L.; writing—original draft preparation, Z.L.; writing—review and editing, Z.L. and P.X.; visualization, L.F.C.; supervision, Y.Z. and Z.J.; project administration, T.L. All authors have read and agreed to the published version of the manuscript.

Funding: This work is supported by the Program of China Scholarship Council (Grant No. 202509290023).

Institutional Review Board Statement: Not applicable.

Informed Consent Statement: Not applicable.

Data Availability Statement: The data underlying the results presented in this paper are not publicly available at this time, but may be obtained from the authors upon reasonable request.

Conflicts of Interest: The authors declare no conflicts of interest.

Abbreviations

The following abbreviations are used in this manuscript:

THz	Terahertz
P-B phase	Pancharatnam–Berry phase

PCR	Polarization Conversion Ratio
RCP	Right-handed circularly polarized
LCP	Left-handed circularly polarized
OAM	orbital angular momentum
GS algorithm	Gerchberg–Saxton algorithm

References

1. Zhang, X.; Wang, Z.; Gong, Y. Progress in multifunctional tunable terahertz metasurface waveplates. *J. Electron. Mater.* **2025**, *54*, 9429–9450. [CrossRef]
2. Zheng, D.; Wu, G.-B.; Jiang, Z.H.; Hong, W.; Chan, C.H.; Wu, K. Enabling beam-scanning antenna technologies for terahertz wireless systems: A review. *Fundam. Res.* **2025**, *5*, 556–570. [CrossRef] [PubMed]
3. Ohkoshi, S.I.; Tsuzuo, Y.; Yoshikiyo, M.; Namai, A.; Otake, T.; Okuzono, K.; Tanaka, Y.; Katayama, S. Ultrathin Terahertz-Wave Absorber Based on Inorganic Materials for 6G Wireless Communications. *ACS Appl. Mater. Interfaces* **2025**, *17*, 9523–9529. [CrossRef]
4. Cui, C.; Gao, X.; Chen, Z.; Yi, Z.; Cheng, S.; Ahmad, S.; Tang, C.; Deng, J. Transient simulation and optimization of planar heat source system based on finite element method. *Mod. Phys. Lett. B* **2026**, *40*, 2650081. [CrossRef]
5. Mu, Y.; Xia, D.; Han, J.; Ma, X.; Wang, X.; Liu, H.; Li, L. Time-space-coding radiation-stealth metasurface with amplitude-phase co-modulation. *Adv. Funct. Mater.* **2024**, *34*, 2407802. [CrossRef]
6. Li, Q.; Zhang, J.; Liu, L.; He, C.; Zhu, W. Graphene-based optically transparent metasurface for microwave and terahertz cross-band stealth utilizing multiple stealth strategies. *Carbon* **2024**, *219*, 118833. [CrossRef]
7. Wang, Q.; Ge, S.; Yu, H.; Hu, W. Liquid crystal integrated dynamic terahertz metalenses. *Laser Photonics Rev.* **2024**, *18*, 2400869. [CrossRef]
8. Jiang, Z.; Chao, M.; Liu, Q.; Cheng, B.; Song, G.; Liu, J. High-efficiency spin-selected multi-foci terahertz metalens. *Opt. Lasers Eng.* **2024**, *174*, 107816. [CrossRef]
9. Carvalho, W.O.; Moncada-Villa, E.; Mejía-Salazar, J.R.; Spadoti, D.H. Dynamic terahertz beamforming based on magnetically switchable hyperbolic materials. *J. Phys. D Appl. Phys.* **2024**, *57*, 175001. [CrossRef]
10. Hao, W.; Shi, H.; Sun, G.; Huang, C. Joint beamforming design for active RIS-aided THz ISAC systems with delay alignment modulation. *IEEE Wirel. Commun. Lett.* **2023**, *12*, 1816–1820. [CrossRef]
11. Zhang, H.; Chen, Z.; Yi, Z.; Cheng, S.; Ahmad, S.; Tang, C.; Deng, J. Three band THz perfect absorption device based on graphene metasurface structure. *Phys. E Low-Dimens. Syst. Nanostruct.* **2026**, *181*, 116542. [CrossRef]
12. Zhang, X.-C. Terahertz Photonic Devices. *Dir. Eng.* **2003**, *2*, 45461.
13. Chen, J.; Shi, D.; Hu, Z.; Tang, B. Tunable Switching of Quasi-bound States in the Continuum in Terahertz Metasurfaces. *IEEE J. Sel. Top. Quantum Electron.* **2025**, *32*, 4700107. [CrossRef]
14. Yang, F.; Xu, H.; Zhu, X.; Wang, D.; Zhang, Y.; Feng, Z. Graphene-based flexible optically transparent dual-tunable metasurface. *Adv. Mater. Technol.* **2024**, *9*, 2301911. [CrossRef]
15. Du, H.; Zhang, X.; Liu, J.; Meng, H.; Feng, H.; Yang, S.; Gao, Y. Graphene-based switchable and tunable selective absorption metasurface. *J. Nanophotonics* **2025**, *19*, 016009. [CrossRef]
16. Fu, P.; Chen, Z.; Yi, Z.; Cheng, S.; Ahmad, S.; Li, B. Graphene-Based Terahertz Perfect Absorber with Broadband, Wide-Angle, and Dynamically Tunable Performance. *Phys. Status Solidi-(RRL)-Rapid Res. Lett.* **2026**, *20*, e70163. [CrossRef]
17. Zeng, N.; Chen, Z.; Yi, Z.; Cheng, S.; Ahmad, S.; Tang, C.; Gao, F.; Li, B. Terahertz multi-band tunable refractive index sensing graphene absorber based on surface plasmon resonance. *Phys. B Condens. Matter* **2026**, *734*, 418608. [CrossRef]
18. Zhang, G.; Li, K.; Xu, L.; Yang, J.; Yin, Z.; Lu, H.; Deng, G.; Li, Y. 32-state liquid crystal programmable metasurface for terahertz phase manipulation. *IEEE Antennas Wirel. Propag. Lett.* **2024**, *23*, 2066–2070. [CrossRef]
19. Valenzuela, C.; Chen, S.; Wang, L. Liquid crystals enable dynamic metasurfaces for transformative optics. *Matter* **2025**, *8*, 102346. [CrossRef]
20. Shi, W.; Feng, H.; Zhang, L.; Zhao, X.; Li, J.; Meng, H.; Jia, Y.; Gao, Y. Multifunctional vortex fields manipulation enabled based on vanadium dioxide metasurfaces. *Photonics Nanostruct.-Fundam. Appl.* **2025**, *66*, 101448. [CrossRef]
21. Cui, Y.; Han, X.; Lei, J.; Zhang, A.; Lu, X. Dual-functional reconfigurable metasurface for reversible circular and linear dichroism. *Photonics Nanostruct.-Fundam. Appl.* **2025**, *65*, 101407. [CrossRef]
22. Yang, F.; Tan, T.C.; Prakash, S.; Kumar, A.; Ariando, A.; Singh, R.; Wang, N.; Pitchappa, P. Reconfigurable Wide-Angle Beam-Steering Terahertz Metasurfaces Based on Vanadium Dioxide. *Adv. Opt. Mater.* **2024**, *12*, 2302047. [CrossRef]
23. Zhou, Q.; Li, Y.; Wu, T.; Qiu, Q.; Duan, J.; Jiang, L.; Mao, W.; Yao, N.; Huang, Z. Terahertz metasurface modulators based on photosensitive silicon. *Laser Photonics Rev.* **2023**, *17*, 2200808. [CrossRef]
24. Jia, M.; Zhao, C.; Wang, H.; Sun, W.; Lu, Y. Flexible terahertz beam manipulation and convolution operations in light-controllable digital coding metasurfaces. *iScience* **2025**, *28*, 111688. [CrossRef]

25. Jin, G.; Zhu, Y.; Yang, H.; Tang, B. Switchable Tri-Functional Terahertz Metamaterial Integrated with Vanadium Dioxide and Photosensitive Silicon. *Nanomaterials* **2025**, *15*, 835. [CrossRef] [PubMed]
26. Wang, G.; Zhang, X.; Liu, J.; Feng, H.; Li, M.; Yang, S.; Jia, Y.; Meng, H.; Gao, Y. A multifunction tunable terahertz chiral metasurface based on graphene and photosensitive silicon. *Opt. Mater.* **2024**, *150*, 115177. [CrossRef]
27. Yu, H.; Sun, X.; Liu, L.; Zhang, Y.; Liu, H.; Jiang, X.; Yu, T. Dynamic Modulation of Terahertz Beams Based on Photosensitive Silicon-Gold Composite Metasurfaces. *J. Electron. Mater.* **2025**, *54*, 3182–3195. [CrossRef]
28. Wang, X.; He, S.; Wang, W.; Duan, X.; Shi, H. Design of a mechanically adjustable multifunctional beam deflection metasurface. *Opt. Express* **2025**, *33*, 26846–26856. [CrossRef]
29. Cheng, Y.; Gong, R.; Zhao, J. A photoexcited switchable perfect metamaterial absorber/reflector with polarization-independent and wide-angle for terahertz waves. *Opt. Mater.* **2016**, *62*, 28–33. [CrossRef]
30. Lu, T.; Wu, J.; Shen, Z.; Wang, Y.; Cheng, H.; Li, Y.; Yang, Y.; Yang, H. Single-layer ultra-wideband multifunctional transmissive metasurface. *IEEE Trans. Antennas Propag.* **2022**, *70*, 6850–6857. [CrossRef]
31. Cui, J.; Qing, C.; Feng, L.; Zhang, D. Exploiting the combined dynamic and geometric phases for optical vortex beam generation using metasurfaces. *Nanophotonics* **2025**, *14*, 635–646. [CrossRef]
32. Jing, X.; Gui, X.; Zhou, P.; Hong, Z. Physical explanation of Fabry–Pérot cavity for broadband bilayer metamaterials polarization converter. *J. Light. Technol.* **2018**, *36*, 2322–2327. [CrossRef]
33. Fu, Y.; Song, Z. Manipulating terahertz wavefront for tri-channel holograms and OAM beams based on diatomic metasurfaces. *Phys. Scr.* **2025**, *100*, 065512. [CrossRef]
34. Zhang, X.; He, X.; Zhang, Y.; Lu, G.; Geng, Z. Mirror-symmetric multi-OAM vortex beam generation with 1-bit interleaved terahertz metasurfaces. *Opt. Laser Technol.* **2025**, *186*, 112606. [CrossRef]
35. Li, S.J.; Han, B.W.; Li, Z.Y.; Liu, X.B.; Huang, G.S.; Li, R.Q.; Cao, X.Y. Transmissive coding metasurface with dual-circularly polarized multi-beam. *Opt. Express* **2022**, *30*, 26362–26376. [CrossRef]
36. Zheng, G.; Mühlenbernd, H.; Kenney, M.; Li, G.; Zentgraf, T.; Zhang, S. Metasurface holograms reaching 80% efficiency. *Nat. Nanotechnol.* **2015**, *10*, 308–312. [CrossRef]
37. Wei, W.; Tang, P.; Shao, J.; Zhu, J.; Zhao, X.; Wu, C. End-to-end design of metasurface-based complex-amplitude holograms by physics-driven deep neural networks. *Nanophotonics* **2022**, *11*, 2921–2929. [CrossRef]
38. Wang, J.; Xiao, Y.; Yang, L.; Wang, D.; Cai, B.; Luo, H.; Cheng, Y. Dual-controlled terahertz tunable broadband metasurface based on photosensitive silicon and vanadium dioxide for multi-functional application. *Phys. Lett. A* **2025**, *556*, 130841. [CrossRef]
39. Dong, G.; Shi, H.; Xia, S.; Zhang, A.; Xu, Z.; Wei, X. Ultra-broadband perfect cross polarization conversion metasurface. *Opt. Commun.* **2016**, *365*, 108–112. [CrossRef]
40. Naghshpour, N.; Pakizeh, T. Hybrid VO_2-graphene bi-functional digital metasurface for beam steering and dual-band absorption. *J. Appl. Phys.* **2025**, *138*, 203103. [CrossRef]
41. Pan, T.; Liu, C.; Peng, S.; Lu, H.; Zhang, H.; Xu, X.; Yang, F. A terahertz programmable digital metasurface based on vanadium dioxide. *Photonics* **2024**, *11*, 527. [CrossRef]
42. Amoateng, E.; Mubarak Sani, E.; Obeng Kwakye, K.S.; Pitilakis, A. Analysis and Design of a Hybrid Graphene/Vanadium-Dioxide Terahertz Metasurface with Independently Reconfigurable Reflection Phase and Magnitude. *Photonics* **2026**, *13*, 195. [CrossRef]
43. Long, Z.; Xu, Z. A Multifunctional Reconfigurable Terahertz Metasurface Enabling Spin-Decoupled Logic Operations and Holography. *Materials* **2025**, *18*, 4362. [CrossRef]